Proceedings of the ASME Turbo Expo 2024
Turbomachinery Technical Conference and Exposition
GT2024
June 24–28, 2024, London, England, United Kingdom

GT2024-124845

SPATIAL TEMPERATURE MEASUREMENTS IN A SWIRL-STABILIZED HYDROGEN-AIR DIFFUSION FLAME AT ELEVATED PRESSURE USING LASER-INDUCED GRATING SPECTROSCOPY

Oussama Chaib[1,†,*], Lee Weller[1,†], Anthony Giles[2], Steve Morris[2], Benjamin A. O. Williams[3], Simone Hochgreb[1],

[1]Engineering Department, University of Cambridge, Trumpington St, Cambridge, CB2 1PZ, United Kingdom
[2]Gas Turbine Research Centre, School of Engineering, Cardiff University, Cardiff, CF24 3AA, United Kingdom
[3]Department of Engineering Science, University of Oxford, Parks Road, Oxford, OX1 3PJ, United Kingdom

ABSTRACT

Laser-induced grating spectroscopy (LIGS) is applied, for the first time, to a swirling non-premixed hydrogen-air flame in a high-pressure combustion facility. A portable LIGS unit is used to probe 35 different axial and radial locations in the flame and a new conditioned processing approach based on laminar flame simulation is introduced to infer temperatures from instantaneous LIGS spectra. Thermal and electrostrictive frequencies are used to produce a spatial map of temperatures in the combustor. Temperatures up to 2,500 K are measured in this work, which constitute the highest temperatures ever measured using LIGS. Challenges associated with the deployment of the technique in turbulent stratified hydrogen flames are discussed, as are potential measures to overcome them, including the use of data-driven clustering techniques.

Keywords: LIGS, Hydrogen flames, High-pressure combustion, Temperature measurements, Time-series clustering

NOMENCLATURE
Symbols

γ	Heat capacity ratio [-]
$\hat{I}_{OH}$	Normalized OH intensity [-]
$\hat{S}$	Normalized power spectral density [-]
$\hat{V}$	Normalized voltage [-]
Λ	Fringe spacing [μm]
λ	Wavelength [nm]
ϕ	Equivalence ratio [-]
ρ	Density [kg m^{-3}]
θ	Crossing angle [°]
θ_B	Bragg angle [°]
υ_s	Local speed of sound [m.s^{-1}]

---

†Joint first authors
*Corresponding author

a	Strain rate [s^{-1}]
d	Diameter [mm]
e	Thickness [mm]
f	Modulation frequency [MHz]
J	Momentum flux ratio [-]
n	Mechanism factor [-]
P_{th}	Thermal power [kW]
R	Universal gas constant [J K^{-1} mol^{-1}]
r	Radial location [mm]
Re	Reynolds number [-]
S	Swirl number [-]
T	Temperature [K]
t	Time [ns]
u	Bulk flow velocity [m s^{-1}]
W	Molecular weight [kg kmol^{-1}]
Z	Bilger mixture fraction [-]
z	Axial location [mm]

Subscripts

c	Calibration
E	Electrostrictive
f	Fuel
h	Hydraulic
ox	Oxidizer
p	Pump
pr	Probe
st	Stoichiometric
T	Thermal
thr	Threshold

Acronyms

CARS	Coherent Anti-Stokes Raman Spectroscopy
GTRC	Gas Turbine Research Center
HPOC	High-Pressure Optical Chamber
IRZ	Inner Recirculation Zone
LIGS	Laser-Induced Grating Spectroscopy
ORZ	Outer Recirculation Zone

PILOT	Portable In-line LIGS for Optical Thermometry
PSD	Power Spectral Density

1. INTRODUCTION

Accurate and non-intrusive spatio-temporal measurements of key scalars such as temperature and species concentrations are of interest in understanding the structure and stability of turbulent flames in high pressure environments. As the global energy landscape shifts its attention to carbon-free alternatives, there is renewed interest in hydrogen-powered combustors especially for hard-to-decarbonize sectors (i.e., shipping, heavy transport and aviation). The unusual properties of hydrogen (i.e., high mass diffusivity, high reactivity and large flame speeds) pose a number of challenges to current combustion systems. They materialize in a propensity to flashback, high thermal loads on the solid parts of the combustor, and flame instabilities, among others [1–3]. This underpins the need for substantial experimental endeavors to understand implications on flame stability and pollutant emissions (i.e., NOx) at high blending ratios and elevated pressures. In addressing some of these challenges, modern-day non-premixed and partially premixed swirl combustors have garnered interest. Flashback risk can indeed be mitigated if fuel and oxidizer streams are separated, while swirl numbers and momentum flux ratios can be tuned to promote mixing and maximize the power density and combustion efficiency [2, 4]. These flames are however known to exhibit complex structures (vortical patterns, recirculation zones, multiple shear layers and reaction zones) due to the interplay between flow dynamics and combustion processes [5, 6]. Further, the presence of stoichiometric zones leads to high temperatures and undesirable elevated NO formation. This reiterates the imperative need for accurate and reliable local and instantaneous optical measurement techniques at high temperatures and representative pressures.

The application of non-intrusive laser-based optical diagnostics for thermometry in flames has been the subject of intense research [7–12]. Various non-intrusive techniques have been developed along the years, each with strengths and weaknesses. Laser absorption techniques are fast, robust, and accurate but lack spatial resolution [11, 12]. Laser-induced fluorescence can achieve good spatial and temporal resolution but requires the presence of a fluorescing species in the probed medium [8, 13]. Precise knowledge of local composition is needed to estimate local quenching cross-sections which limits the scope of the technique for the given application. Rayleigh scattering is another alternative which provides good spatial (planar) or temporal (point-based) resolution but requires high laser energies and extensive denoising and calibration [14–17]. Finally, non-linear four-wave mixing techniques such as Coherent Anti-Stokes Raman spectroscopy (CARS) can achieve high signal-to-noise spatio-temporal measurements but require specialized narrow-band lasers, complex optical arrangements, and advanced post-processing algorithms [18]. Laser-induced grating spectroscopy (LIGS) is a simpler and less costly non-linear alternative. The technique is especially suited for measurements in high-pressure environments, and is capable of delivering precise, highly-accurate, point-based temperature measurements in flames [19–25].

To date, most LIGS thermometry applications have been limited to homogeneous laminar or turbulent environments. Applications in non-reacting gas flows constitute a substantial body of the existing literature, while applications in flames are somewhat

limited. In the latter, the potential of the technique has mainly been demonstrated in laboratory-scale laminar premixed flames, not representative of flames encountered in practical gas turbine applications [24, 26–28]. The potential of the technique in turbulent swirl flames in a high-pressure gas turbine was only recently demonstrated by Weller et al. [29]. The study employed a portable LIGS unit [30], equipped with a 2–axis translation stage to probe different axial and radial locations in the combustor. Spatial (24 axial/radial locations), instantaneous (ns) temperature and water molar fraction measurements were hence obtained in a swirling premixed methane-air flame at 3 bar, extending the application of the technique to premixed swirling flames at elevated pressure, both in the reactant and product zones. The viability of the diagnostic is yet to be demonstrated in non-premixed configurations where the complex flame structure and presence of multiple mixing layers may challenge the performance of the diagnostic. Additionally, and in light of the increasing interest in hydrogen-fuelled combustion technology, there is a pressing need to examine the technique's long-term suitability for thermometry in such high-temperature stratified environments.

In this work, we demonstrate the first application of LIGS to the unexplored non-premixed flame configuration. Measurements are conducted in a hydrogen-air swirl flame at elevated pressure (3 bar) in a gas turbine research facility (the GTRC, in Port Talbot, UK). The *Portable In-line LIGS for Optical Thermometry* (PILOT) unit [30] is used to probe 35 different axial and radial locations in the combustor. A particular novelty of the study is the measurement of pure hydrogen LIGS spectra, which is hereby achieved for the first time. A new conditioned post-processing approach based on 1D laminar flame simulation is used to infer temperatures from instantaneous LIGS spectra and produce a two-dimensional temperature map of the diffusion flame. Results show that LIGS can be successfully applied to measure temperatures in non-premixed flame configurations at industry-relevant conditions. Precision is highest in the hot products region where temperatures up to 2,500 K are measured. The unique properties of hydrogen limit the performance of the technique in the cold fuel-rich side of the flame. Challenges and implications for future work are discussed, including the use of machine learning and data-driven techniques for LIGS thermometry in turbulent stratified environments.

The paper is organized as follows : following a brief introduction to LIGS theory (Section 2), descriptions of the experimental facilities and diagnostics are provided (Section 3). Numerical and experimental results are presented in Section 4. Challenges and implications for future experimental design and post-processing are finally discussed in Section 5.

2. THEORY

In a typical LIGS experiment, a monochromatic pulsed laser beam (the pump) is used to generate two coherent pulses which are subsequently overlapped. The interference of the two coherent beams induces local, periodic variations of the refractive index in the intersection region called the probe volume. A laser-induced stationary diffraction grating is formed in the process, with a fringe spacing Λ related to the crossing angle of the incident

beams θ and the pump laser wavelength λ_p:

$$\Lambda = \frac{\lambda_p}{2 \sin(\theta/2)} . \tag{1}$$

A coherent beam (the probe), typically long-pulse or continuous wave, is then aligned to intersect the grating at the Bragg angle θ_B:

$$\theta_B = \sin^{-1}\left(\frac{\lambda_{pr}}{2\Lambda}\right) . \tag{2}$$

where λ_{pr} is the wavelength of the probe. A small fraction of the probe laser is diffracted off the grating and forms the LIGS signal. The modulation frequency in the probe volume is encoded in the latter and is proportional to the local speed of sound v_s in the medium :

$$f = n\frac{v_s}{\Lambda} = 2n\frac{v_s}{\lambda_p} \sin(\theta/2) , \tag{3}$$

where $n \in \{1, 2\}$ is a proportionality factor referring to the mechanism behind grating formation. The resonant ($n = 1$) process is thermalization and is the result of the non-adiabatic collisional excitation and subsequent quenching of the absorbing molecules in the probe volume. It is hence conditional on the presence of absorbing species (at the given pump laser wavelength) in the medium. The non-resonant ($n = 2$) process is electrostriction and is the result of an adiabatic interaction with the dielectric medium in the probe volume at sufficiently high pump pulse energies [19, 20].

The speed of sound is related to the local thermo-physical properties in the medium. In ideal gases, the following equality is satisfied :

$$v_s = \sqrt{\frac{\gamma R T}{W}} , \tag{4}$$

where γ is the heat capacity ratio, R is the ideal gas constant, T is the temperature, W is the molecular weight of the gas mixture in the probe volume.

The fringe spacing can be determined by calibration in a reference gas of known thermo-physical properties. It can be obtained by measuring the modulation frequency in the LIGS signal and combining Eqs. 3, and 4:

$$\Lambda = \frac{n_c}{f_c}v_{s,c} = \frac{n_c}{f_c}\sqrt{\frac{\gamma_c R T_c}{W_c}} , \tag{5}$$

where the subscript $<.>_c$ refers to calibration data. Calibration data can be used to eliminate the fringe spacing dependency in Eq. 5, yielding a simplified expression for temperature in any probed medium :

$$T = \frac{\gamma_c/W_c}{\gamma/W}\left(\frac{n_c/f_c}{n/f}\right)^2 T_c . \tag{6}$$

Ambient air ($n_c = 2$) is typically used as the reference medium with relatively high precision in calibration frequency measurement [29, 30]. It was hence used for calibration in this study ($T_c = 285 \pm 2$ K, $\gamma_c = 1.4$, $W_c = 28.97$ g.mol^{-1}) which yielded an electrostrictive frequency of $f_c = 34$ MHz measured experimentally from corresponding LIGS spectra. It is important to note that the accuracy of temperature measurements using LIGS

Copyright © 2024 by ASME

is heavily dependent on the accuracy of the γ/W estimates in Eq. 6. While this factor remained relatively constant in a past investigation by the authors employing lean methane-air flames [29] (due to the abundance of nitrogen), it is expected to change drastically in this study due to the non-premixed geometry and the large differences in molecular weight between hydrogen and air. We elaborate further on this matter in section 4.1.

3. EXPERIMENTAL METHODS

3.1 High-pressure combustor rig

A high-pressure optical chamber (HPOC) houses the combustor. The HPOC has two outer one-inch thick rectangular Spectrosil windows (either side) which allow optical access to the flame. The latter is confined in a cylindrical quartz tube (3.5 mm thickness) with 100 mm inner diameter and 600 mm length containing five identical sets of holes located at axial positions $z = 15$ mm, 35 mm, 55 mm, 75 mm and 95 mm from the gas inlet plane. These slits are rectangular (4×4 mm^2, length $\times$ width) with rounded corners on the upstream and downstream ends (2 mm radius). They were necessary due to the curvature of the cylindrical quartz chamber, which prevented direct laser access to the flame. The combustor is a non-premixed coaxial jets burner with central (fuel) and annular (air) inlet diameters of $d_f = 18$ mm and $d_{ox} = 40$ mm, respectively. Hydrogen at ambient temperature ($T_f = 294.7 \pm 2.5$ K) enters the chamber through the central injector (lip thickness $e = 3.5$ mm) while the annular air stream is preheated at a temperature of $T_{ox} = 501.7 \pm 4.1$ K, both measured by thermocouple. A swirling motion is imparted to the preheated air flow using a nine-blade axial swirler of geometric swirl number $S = 0.8$.

The experiments presented in this study are carried out at 3.0 ± 0.1 bar absolute pressure under a global equivalence ratio of $\phi = 0.5$, a thermal power of $P_{th} = 34.1$ kW, and a momentum flux ratio $J = 59$. The annular Reynolds number based on the hydraulic diameter of the air inlet ($d_h = 15$ mm) is $Re = 13,980$. This resulted in a relatively compact symmetric flame anchored to the injector lip which acts as a bluff body. Detailed conditions are compiled in Table 1. For a comprehensive description of the experimental rig and design, the reader can refer to the authors' previous works [29, 31–33].

3.2 OH* chemiluminescence

Chemiluminescence images of the excited hydroxyl radical OH* (wavelength $\lambda = 310$ nm) are acquired using a high-speed camera (Phantom v1212 CMOS) with a high-speed intensifier (SIL40HG50) equipped with a UV lens (focal length 78 mm, $f/11$ f-stop) and a narrow bandpass filter (315 ± 15 nm). The imaging field-of-view is 100×100 mm^2 with a resolution of approximately 0.2 mm per pixel. Over 2000 background-corrected OH* chemiluminescence images were acquired (frame rate 4 kHz, gate time 10 μs) to construct mean chemiluminescence fields. We note the chemiluminescence and LIGS data were not acquired simultaneously.

3.3 PILOT unit

Figure 1 shows the PILOT unit along with the quartz tube and back-end collection optics. The PILOT unit [30] is used to perform tracer-free electrostrictive and water-thermal LIGS measurements in the HPOC. The layout is identical to the one used by Weller et al. in a previous campaign [29]. The system (Nd:YAG Quantel Merion C laser) produced pump beams at 1064 nm with repetition rates of 20 Hz and energies of 35 mJ per 10 ns pulse. The probe beam at 532 nm (Verdi V-18 laser from Coherent) delivered a continuous laser beam with a power of 10 W.

The PILOT unit and collection optics were mounted on a 2-axis (radial: r, axial: z) motorized translation stage at the front and back-end of the HPOC. This stage was fixed onto a single platform attached underneath the HPOC to minimize the effects of vibrations during rig operation. This also ensured that the collection optics could be translated in tandem with the beam delivery unit during the investigation.

The optical arrangement of the PILOT unit produces a spatial resolution of $6 \times 0.3 \times 0.3$ mm^3 (radial, axial, azimuthal) corresponding to the probe volume. The two shorter dimensions correspond to the Gaussian beam diameters, and the longer lengthwise dimension along the radial direction is a result of the long interaction length between the two pump beams and the probe beam. This limitation arises from the need to bring in the light through a small diameter lens from one side of the combustion chamber. The motorized translation stages are used to collect LIGS signals across a wide range of axial locations ($z = 15, 35, 55, 75, 95$ mm) corresponding the position of the slits on the quartz chamber. Only positive radial positions ($r = 0, 10, 20, 30, 40, 50, 60$ mm) are scanned in this study (the symmetric nature of flames produced by this burner has been demonstrated extensively in past studies [31–33], and more recently by Weller et al. [29]). This enables measurements in the shear layers as well as the central and outer recirculation zones (IRZ and ORZ, respectively).

A Hamamatsu H10721-20 photomultiplier tube and a photodiode (Thorlabs DET210) are used to collect the signal and pump beams, respectively. The acquisition of the LIGS signal was then triggered by the pump beam on a 4-channel Teledyne LeCroy 6104A High Definition oscilloscope (12-bit channel at 10 GHz). The signal-to-noise ratio of the LIGS signals was improved by introducing a spatial filter along the detection rail. This helped minimize any reflected light from the HPOC windows and quartz tube.

LIGS spectra are acquired at each axial/radial location at 20 Hz for a total duration of 50 s per location. Over 1,000 spectra (each being a voltage vs. time signal with 20,002 data points) are collected at each location. Raw signals are filtered using a low-pass Butterworth filter to eliminate high-frequency noise then normalized by maxima. A similar approach to that used in Weller et al. [29] is followed to measure frequencies of LIGS spectra. A Hamming window is first applied to individual signals to reduce spectral leakage and these are subsequently zero-padded to 2^{19} points. Frequencies are inferred from the power spectral density (PSD) of LIGS spectra using a peak finding function with a minimum peak prominence set to 0.01.

4. RESULTS

4.1 Laminar flame simulations

A first exploratory study is conducted using one-dimensional laminar flame simulations of steady, one-dimensional counter-
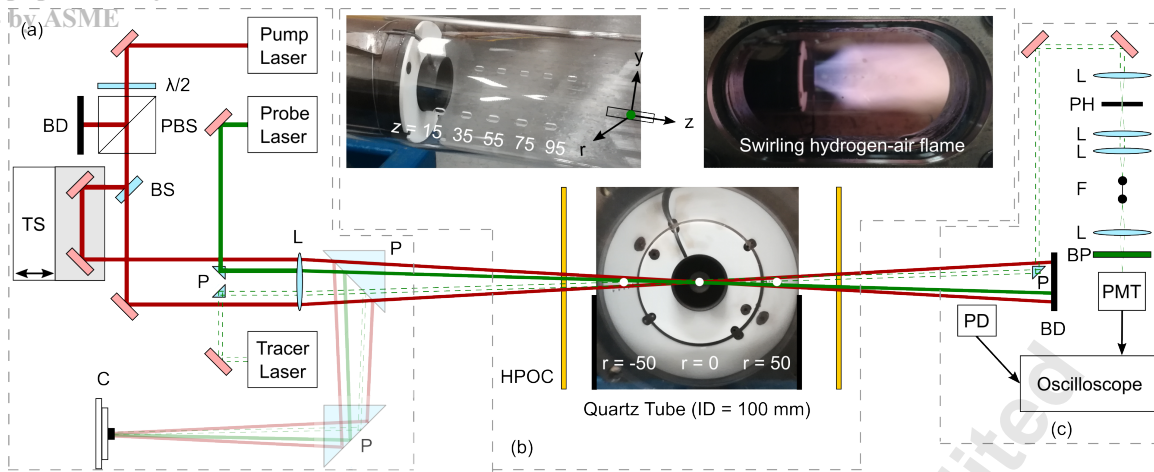
Figure 1: Schematic of (a) the PILOT unit, showing the path of all three (pump, probe and tracer) beams, along with (b) a schematic of the cylindrical quartz tube and (c) back-end collection optics. Pump: 1064 nm pulsed laser; Probe: 532 nm continuous wave laser; Tracer: 532 nm diode pump solid state laser; $\lambda/2$: Half-Wave Plate; PBS: Polarisation Beam Splitter (for 1064 nm); TS: Translation Stage; BS: Beam Splitter (for 1064 nm); P: Prism; C: Camera; L: Lens; PD: Photodiode; BD: Beam Dump; PH: Pin Hole; F: Fiber; BP: Band-Pass Filter (for 532 nm); PMT: Photomultiplier Tube.

Dataset	p (bar)	T_f (K)	T_{ox} (K)	ϕ (-)	u_f (m.s^{-1})	u_{ox} (m.s^{-1})	P_{th} (kW)	J (-)	S (-)	Re (-)
H$_2$-air (diffusion)	3	294.7 ± 2.5	501.7 ± 4.1	0.5	4.54	11.9	34.1	59	0.8	13,980

Table 1: Experimental conditions of the study. Bulk flow velocities u of fuel and oxidizer streams are provided. The momentum flux ratio J is measured as the ratio of air to fuel momentum fluxes $J = \rho_{ox} u_{ox}^2 / \rho_f u_f^2$.

flow hydrogen-air diffusion flames via Cantera [34]. The goal is to examine the structure of the hydrogen-air diffusion flame at hand, and how the relevant quantities (γ/W, f, and T) vary along the flame brush. A kinetic scheme based on the Creck Syngas (H$_2$/CO) high-temperature mechanism (21 species, 62 reactions) is used [35–37]. For the given experimental conditions, the maximum strain rate ahead of the stagnation point, on the oxidizer side, is approximately $a \approx 5,300$ s^{-1}. The results are presented in Fig. 2. The profile of the thermal variable of progress c_T peaks at the stoichiometric mixture fraction $Z_{st} = 0.032$ ($\phi = 1$) and separates the domain into a lean ($Z < Z_{st}$) and rich ($Z > Z_{st}$) region. The γ/W ratio varies quasi-linearly with the mixture fraction from 0.048 mol.g^{-1} in the air stream to 0.70 mol.g^{-1} in the hydrogen stream, which is effectively a factor of 14.6 (note the semi-logarithmic scale of the graph in Fig. 2). It is worth noting this ratio is largely governed by molecular weight in this study as the heat capacity ratio barely varies across the mixture (below 4.2%). A model of temperature vs. electrostrictive frequency is provided in the same figure. This model was constructed by solving Eq. 6 for the electrostrictive frequency f_E ($n = 2$) using the temperature and γ/W values obtained numerically along the axial coordinate of the laminar flame.

The behavior on the lean side is qualitatively similar to that of a lean premixed flame. The abundance of air in this region results in relatively low variation in molecular weight (±7%), and hence a quasi-constant γ/W ratio. Frequencies in this region are comparable to those measured previously by Weller et al. [29] in a lean ($\phi = 0.6$) premixed swirling methane-air flame at 3 bar ($f_E \in [45, 90]$ MHz). Temperatures increase quasi-linearly with

frequency, with the highest expected to be of the order of 2,500 K, corresponding to an electrostrictive frequency of $f_E = 104$ MHz. These are well above the highest temperatures ever measured using LIGS and are significantly larger than those previously measured by Weller et al. ($T_{ad} = 1,818$ K) [29].

The highest frequencies occur on the rich side of the flame, where they can reach values as high as $f_E = 134$ MHz. This exceeds the range of frequencies measured in past investigations, including that of Weller et al. [29], and represents a challenge for the accuracy and robustness of the LIGS diagnostic. Moreover, an unusual behavior is observed in this rich region as temperatures decrease with increasing frequency. This observation is in contrast with the usual positive correlation between temperature and frequency observed in past LIGS studies of premixed flames. It is hence important to note that high frequencies are not equivalent to high temperatures in non-premixed configurations. The high frequencies on the rich side in this study are, instead, due to the low molecular weight of hydrogen which has a corresponding increasing effect on the local speed of sound, as per Eq. 4. Additionally, the high molecular diffusivity of hydrogen in this region results in a much rapid change in temperature with frequency, as evidenced by the steeper negative slope of the curve in this region. Consequently, the large gradients in molecular weight between the stoichiometric hydrogen-air flame and the cold hydrogen mixture result in significantly larger variations in the γ/W ratio.

In absence of spatially-resolved estimates of γ/W, the model obtained from the 1D laminar simulation can be used to infer temperatures from LIGS frequencies measured experimentally,
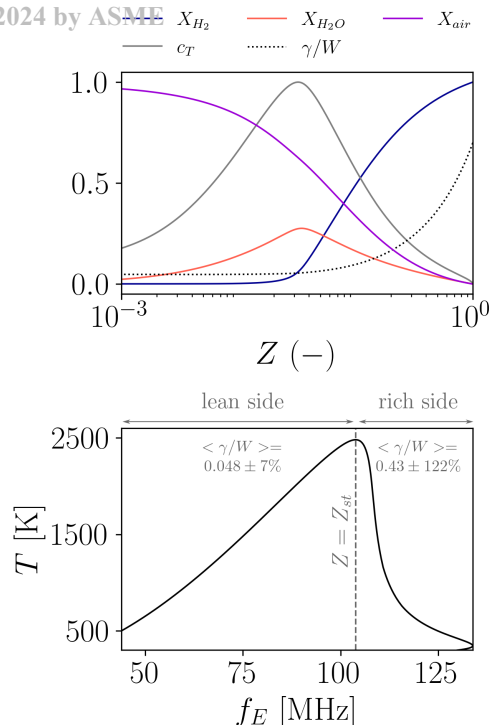
5

Figure 2: Results of the 1D laminar flame simulation. (Top:) Molar fractions of major species X alongside the thermal variable of progress c_T and the γ/W ratio as a function of the Bilger mixture fraction Z (in semi-logarithmic scale). (Bottom:) Temperature as a function of electrostrictive frequency along the simulated flame. The stoichiometric mixture fraction Z_{st} separating the lean and rich sides is marked using the dashed vertical line. Mean values of γ/W in each region are provided with their corresponding 95% confidence intervals (± two standard deviations).
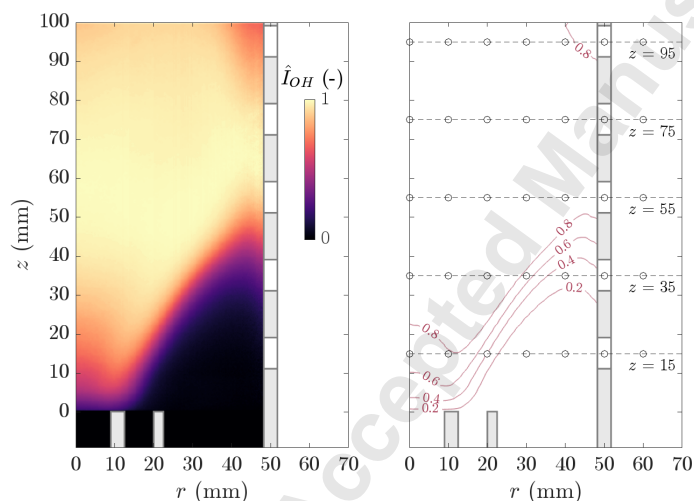

Figure 3: (Left:) Mean OH* chemiluminescence image of the half-flame. Chemiluminescence intensity is normalized to the $\hat{I}_{OH} \in [0; 1]$ range. (Right:) Spatial mapping of axial and radial measurement locations with representative isolines of $\hat{I}_{OH}$.

by interpolation. This approach is used in the remainder of the study to estimate temperatures from LIGS spectra frequencies, with further details in sec. 4.5. Uncertainties are expected to be lowest on the lean side, where the ratio γ/W is relatively constant ($0.05 \pm 7\%$), and largest in the rich side where it varies significantly ($0.43 \pm 122\%$). This highlights one of the main challenges associated with LIGS of hydrogen-air flames in a non-premixed configuration.

4.2 OH* chemiluminescence mapping

Figure 3 illustrates the mean OH* chemiluminescence image of the half-flame and the measurement locations. The flame displays the typical V-shape of a swirling flame anchored on the injector rim. The primary reaction zone is located at the interface of the non-reacting hydrogen and air jets and stretches to a maximum height of 40 to 50 mm before reaching the inner surface of the cylindrical quartz chamber. The outer recirculation zone (ORZ) away from the shear layer and near the wall occupies a much smaller volume. The flame appears relatively close to the walls when $z \geq 50$ mm which may cause a partial leakage of hot combustion products through the slits of the quartz chamber. The chemiluminescence intensity profile displays a concave dome-like shape near the centerline. The width of the $\hat{I}_{OH} = 0.8$ isoline at this location is comparable to the injector radius. This is due to the incoming hydrogen stream whose strong penetration suggests a relatively weak central recirculation zone (IRZ) sufficiently far from the injector rim. This structure is consistent with a non-premixed coaxial jets configuration at high momentum flux ratio when no swirl is conferred to the central fuel flow [4]. Measurement locations cover all relevant regions across the flame. The $z = 15$ and $z = 35$ mm axial positions give access to regions in the ORZ and reactant streams while axial locations further downstream give access to the IRZ and combustion products region.

4.3 LIGS spectra

Examples of characteristic LIGS spectra recorded experimentally at four different locations are provided in Fig. 4. The locations and spectra are selected to reflect the conditions near the respective reactant inlets (hydrogen and preheated air), in the post-combustion zone (products), and in the outer recirculation zone, consistent with the structure of the flame from OH* chemiluminescence (Fig. 3). They are arranged in decreasing order of mixture fraction (from fuel to oxidizer).

A first observation can be made on the decay rate of the spectra which decreases with decreasing mixture fraction. The hydrogen and products spectra are the shortest with durations over 50 and 100 ns, respectively, and decay after 4 or 5 oscillations. The spectra in the ORZ and preheated air stream exhibit at least twice as many oscillations with durations over 200 and 400 ns, respectively. The largest frequencies are hence observed in the hydrogen-rich side, consistent with results of the 1D simulations. The hydrogen spectrum is purely electrostrictive and exhibits a prominent peak at $f_E = 130.7$ MHz which yields a temperature of $T = 304.7$ K using the model obtained previously (Fig. 2). A second less prominent peak appears at $f_E = 74.4$ MHz which is harder to interpret. The corresponding temperature is signif-
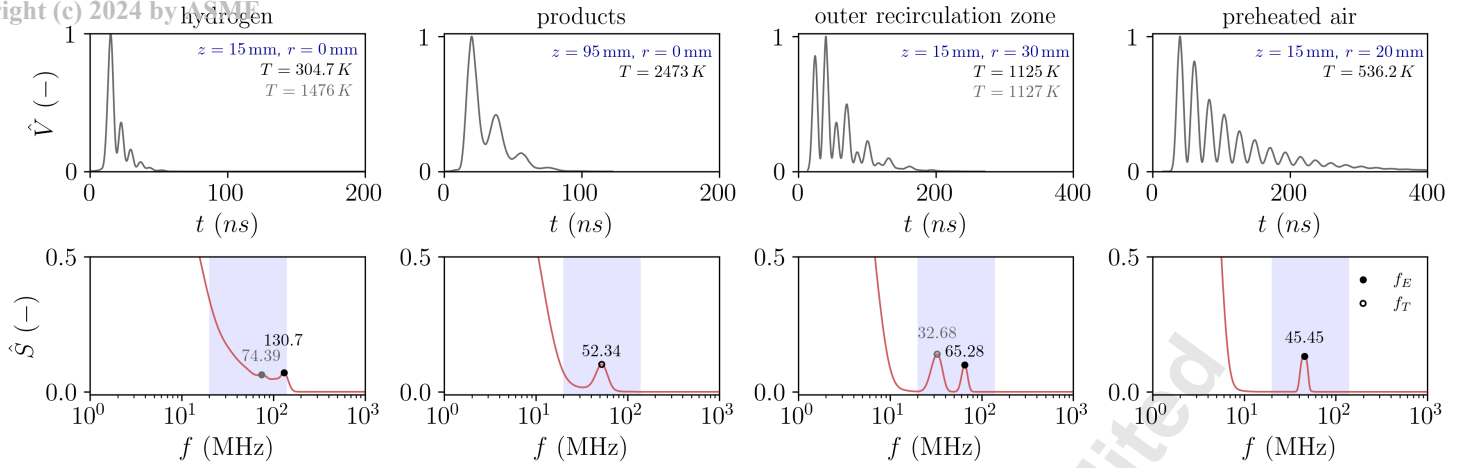
Figure 4: Examples of representative mean LIGS spectra and their PSDs at four different locations. (Top:) LIGS spectra in normalized voltage $\hat{V}$ vs. time format. (Bottom:) Corresponding normalized PSDs $\hat{S}$ as function of frequencies (in semi-logarithmic scale). The expected range of frequencies according to 1D simulations is highlighted in blue color. Electrostrictive and thermal peaks are indicated using filled and unfilled circles respectively. Temperatures measured from the highlighted frequencies are provided next to the corresponding LIGS spectra, in corresponding colors.
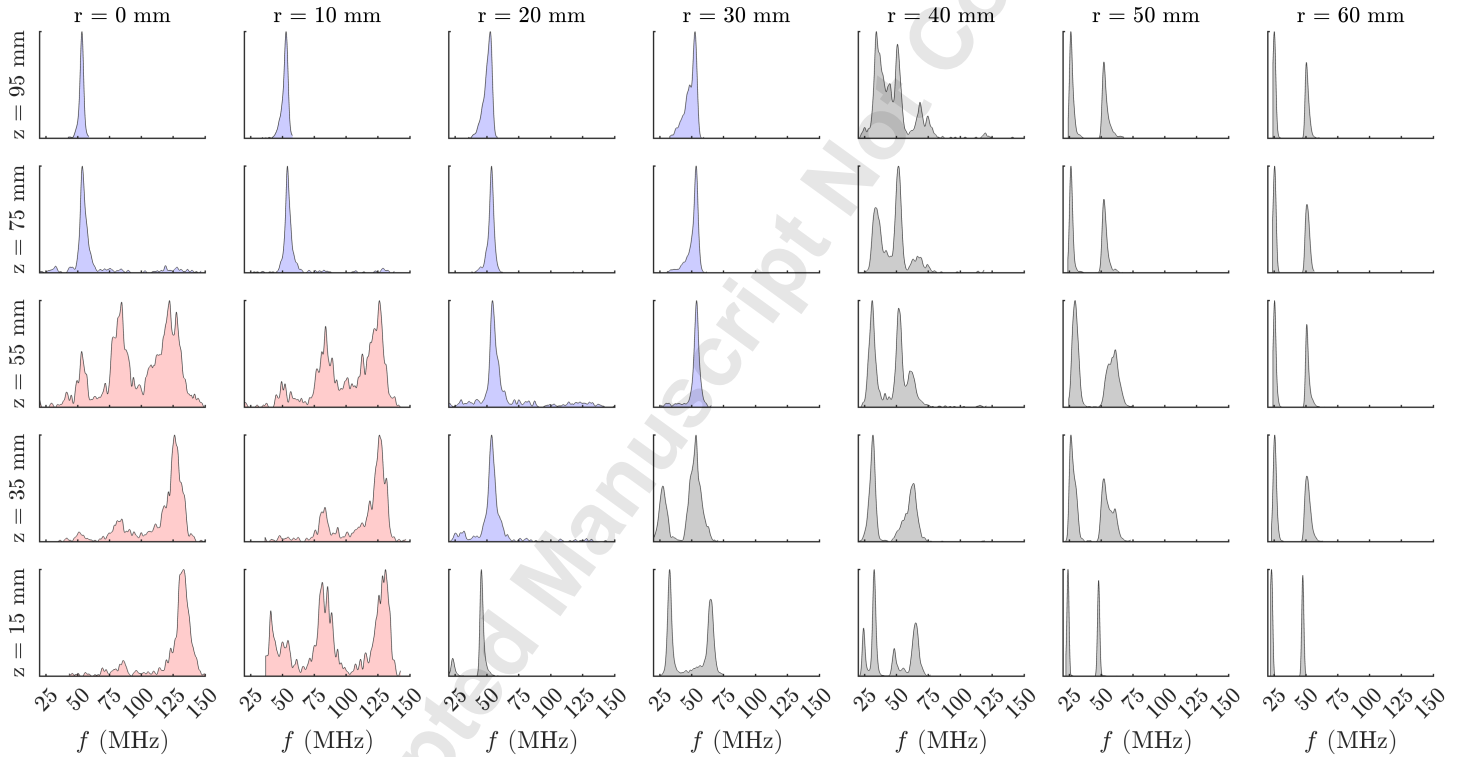

Figure 5: Spatial map of frequency probability density histograms at 35 locations across the combustor. Probability densities are normalized to the [0; 1] range for visibility, with bin widths of 0.25 MHz. Histograms corresponding to lean and rich regions are colored in gray and red, respectively. The products' region is highlighted in blue color.

icantly higher ($T = 1,476$ K) which implies it is likely due to a mixture of reactants and hot products convected by the swirling motion into the probe volume. One notable feature is the broadband shape of the PSD which is a direct consequence of the short duration of the LIGS spectrum and the low number of oscillations (time-frequency uncertainty). This trade-off is well-known in LIGS literature [24, 25] and likely due to the unique proper-

ties of hydrogen in the study at hand. While the laser energy is large enough to generate a 400 ns high signal-to-noise ratio electrostrictive signature in air, it appears insufficient to generate a hydrogen LIGS signature of comparable quality. This behavior was mostly observed in the rich, hydrogen-containing regions of the flame which induces additional uncertainties in measuring characteristic frequencies at these locations. These issues are less

7

pronounced in the products spectrum (Fig. 4) where only a thermal signature is recorded ($f_T = 52.34$ MHz), yielding a temperature of $T = 2,473$ K, close to the stoichiometric flame temperature obtained in the simulation. This is, to the authors' best knowledge, the highest temperature ever measured using LIGS, making it an ideal technique for temperature measurements in hydrogen flames. Only the spectrum in the ORZ features both thermal and electrostrictive peaks, mirroring the change in the magnitude of every other peak in the corresponding LIGS spectrum. This is due to the simultaneous presence of hot air and absorbing water molecules in the probe volume, as well as the larger duration and number of oscillations which mitigates spectral leakage effects. The thermal frequency is approximately half the electrostrictive, as expected, and they both yield a moderate temperature of approximately $T \approx 1,126 \pm 1$ K. The preheated air spectrum features the narrowest PSD peak and exhibits a purely electrostrictive signature of frequency $f_E = 45.45$ MHz. The obtained temperature ($T = 536.2$ K) is slightly above the air preheating temperature.

4.4 Spatial frequency histograms

Frequency histograms are constructed from thermal and electrostrictive frequencies of LIGS spectra at each of the 35 locations and are presented in Fig. 5. This spatial map can be divided into three distinct regions:

1. *The rich region*, shown in red color, is composed of a mixture of hydrogen and hot combustion products. Due to the short duration of the spectra and low signal-to-noise ratios, uncertainties in determining the oscillation frequencies are largest, as mentioned previously. This is evidenced by the noisier histogram and the relatively wide peaks. Three characteristic signatures are present: an electrostrictive hydrogen signature ($f_E > 100$ MHz), an electrostrictive product signature ($67 < f_E \leq 100$ MHz), and a thermal product signature ($f_T \leq 67$ MHz).

2. *The products region*, shown in blue color, is composed of hot combustion products rich in water vapor. This region is dominated by a single thermal peak. These peaks are relatively narrow due to high signal-to-noise ratios in the products with lower fluctuations in local species at these locations. Peaks in this region are slightly above the thermal frequency of the stoichiometric flame temperature by 1 to 3 MHz approximately.

3. *The lean region*, shown in gray, is the most complex and contains a mixture of air and combustion products at variable temperatures. All locations in this region feature a mix of thermal and electrostrictive signatures. Signals collected at a sufficient distance from the reaction zone feature only two peaks: a thermal peak below 42.5 MHz and its corresponding electrostrictive peak above that threshold and at approximately twice the frequency. This is consistent with the results of Weller et al. [29] who used a similar threshold to classify peaks as thermal or electrostrictive prior to computing temperatures. At the location ($z = 15$ mm, $r = 40$ mm), two competing LIGS signatures are present simultaneously: (a) $f_{T,1} = 24.37$ MHz, $f_{E,1} = 48.37$ MHz,

and (b) $f_{T,2} = 32.62$ MHz, $f_{E,2} = 66.12$ MHz, which echoes past observations by Weller et al. at the same radial location [29]. These signatures appear to be a combination of adjacent ones at ($z = 15$ mm, $r = 30$ mm) and ($z = 15$ mm, $r = 50$ mm), and could be due to a hotter ($\Delta T \approx 545$ K) mix of air and combustion products periodically convected into the probe volume by recirculation in the ORZ. This could also be due to the uncertainty in the position of the measurement (approximately 6 mm radially) due to the spatial resolution of the PILOT unit [29].

The most challenging spectra in the lean region are those close to the reaction zone which feature a harmonically-related thermal/electrostrictive signature well separated by the 42.5 MHz threshold, and an additional thermal peak near 50 MHz. At the location ($z = 55$ mm, $r = 40$ mm), for example, the histogram is composed of a thermal/electrostrictive signature ($f_T = 31.12$ MHz and $f_E = 62.12$ MHz) and a thermal peak associated with combustion products at $f_T \approx 52$ MHz. The latter is relatively close to and partially overlaps with the electrostrictive peak. In this case, identifying a definitive and unambiguous threshold to distinguish thermal and electrostrictive frequencies becomes challenging due to their close proximity and potential overlap.

4.5 Conditioned approach for temperature estimation

To compute corresponding temperatures, frequencies have to be classified as thermal or electrostrictive such that the proportionality factor n can be correctly assigned. A similar thresholding approach to that of Weller et al. [29] was used here for this purpose. However, the choice of threshold level does depend on the region considered due to the non-premixed nature of the configuration. A conditioned approach is hence used to improve and adapt the original thresholding method to the diffusion flame geometry. Typically, up to 2 frequencies appear on each individual LIGS spectrum. In the *rich* and *products* regions, a threshold $f_{thr} = 67$ MHz is set to separate the thermal $f_T \leq f_{thr}$ and electrostrictive peaks $f_T > f_{thr}$. This threshold corresponds to the maximum thermal frequency according to the 1D simulations and coincides nicely with the valley between the thermal and first electrostrictive peaks (i.e. at the location $z = 15$ mm, $r = 10$ mm). In the *lean* region, the complexity of LIGS signatures calls for a more developed approach. Two cases emerge :

- **Case 1** : Only harmonically-related frequencies are present in the histogram (i.e. at the location $z = 15$ mm, $r = 30$ mm or $r = 40$ mm). A threshold close to that of Weller et al. [29] is used: $f_{thr} = 42.5$ MHz.

- **Case 2** : An additional thermal peak is present (i.e. at the location $z = 75$ mm, $r = 40$ mm or $z = 95$ mm, $r = 40$ mm). The classification is done on a signal-by-signal basis:

    - When a single frequency is present in the signal, the threshold $f_{thr} = 67$ MHz is used for classification.

    - When two frequencies are present, the ratio of the largest to the smallest is computed to check if they are harmonically related.
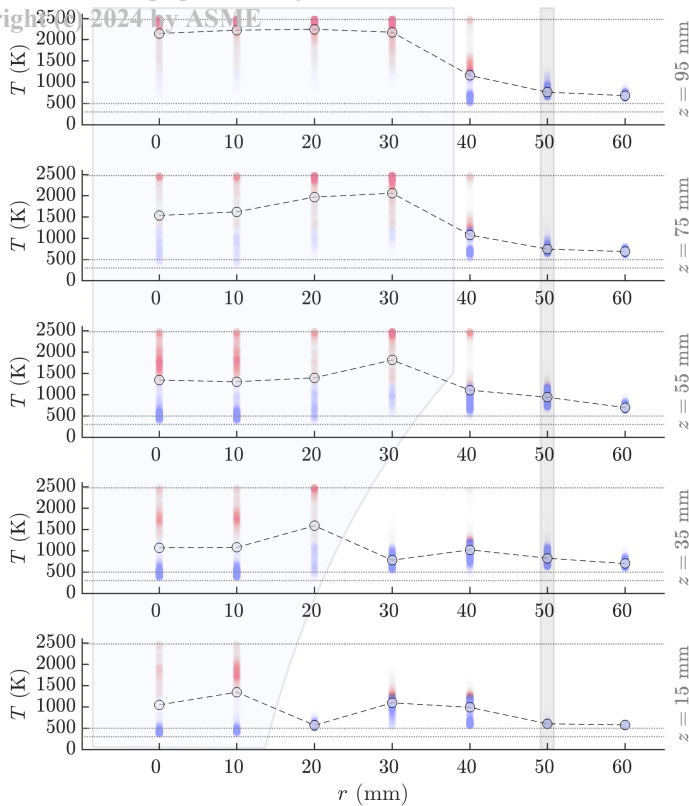
Copyright © 2024 by ASME

Figure 6: Spatial map of temperatures measured at each location. Colored scatter points represent the raw temperatures measured from LIGS frequencies. They are color-coded in red and blue to reflect the different modes at each location. Color intensity indicates the probability density of each temperature. Unfilled circles represent the mean temperature at each location. Dotted horizontal lines highlight the temperatures at the reactant inlets T_f and T_{ox} for hydrogen and air, respectively, and the stoichiometric flame temperature $T_{st} = 2,480$ K. The location of the flame based on these temperature measurements and the wall of the combustion chamber are overlaid in dim gray color.

* If the ratio is within the tolerance range $n = 2 \pm 0.1$, the frequencies are harmonically related and can be classified as thermal and electrostrictive based on their relative magnitudes.
* If the ratio is outside this range, the $f_{thr} = 67$ MHz is used to classify the frequencies as thermal or electrostrictive.

After classifying frequencies as either thermal or electrostrictive, temperatures are estimated from the 1D laminar flame model described previously in sec. 4.1 by interpolation at the corresponding electrostrictive frequency. This approach was found to be both efficient and repeatable, producing consistent results across all locations.

4.6 Spatial temperature measurements

A spatial temperature map at the 35 different locations is provided in Fig. 6. The main flame surface contains a broad spectrum of temperatures, spanning the range $T \in [300; 2,500]$ K while

temperatures elsewhere are moderate with relatively low fluctuations locally. At the lowest axial position ($z = 15$ mm), mean temperatures in the flame are between 1,000 and 1,350 K and only slightly above those in the ORZ. The temperature peaks in the wake of the inner shear layer separating the hydrogen and air streams ($r = 10$ mm) and dips near the burner centerline due to the incoming ambient pure hydrogen stream leaving the injector. The distributions in the highlighted flame region are bimodal, with a dominant peak at 400 K (hydrogen stream) and a second smaller and broader peak centered around 1,800 K. The lowest temperature is right above the air inlet ($r = 20$ mm) and is only slightly above the preheating temperature of the air stream ($T \approx 566.4$ K). The spread in temperatures inside the flame is largest at $z = 55$ mm. Large fluctuations in local stoichiometry are expected at this axial location due to its proximity to the shear layer separating the central fuel stream and the IRZ, where hydrogen burns with vitiated hot air. The temperature at the quartz tube ($z = 55$ mm, $r = 50$ mm) is highest among all the other axial positions, which also gives a rough estimate of the height of the primary hydrogen/air reaction layer and is consistent with the mean OH* chemiluminescence image (Fig. 3). At the highest axial position ($z = 95$ mm), the temperature profile flattens indicating a well-mixed and homogeneous combustion product region with mean temperatures slightly below the stoichiometric flame temperature $T \in [2,100; 2,250]$ K. Temperatures measured outside the chamber are between 570 and 700 K. They increase with height which implies a partial leakage of combustion products through the small slits in the quartz tube, similar to the results obtained previously using a cylindrical stainless steel tube for confinement [29].

5. DISCUSSION

The application of LIGS for temperature measurements in a swirling hydrogen-air diffusion flame at pressure was successfully demonstrated in this work. Some challenges emerged in the process, which warrants attention for future improvements:

* *Hydrogen electrostriction*: The duration of the pure hydrogen electrostrictive signal is relatively short ($t \le 50$ ns) and unideal for high-accuracy measurements in the rich side of the flame. Lower signal decay rates can be achieved using higher pump pulse energies (> 35 mJ) to produce high-precision results in the hydrogen side. Energies should however remain below the ionization threshold to avoid unwanted laser-induced optical breakdown which induces additional uncertainties due to plasma formation [25], as well as low enough to avoid hydrogen ignition so the non-invasive nature of the technique is retained.

* *Frequency-to-temperature conversions*: Local temperatures are estimated using the results of 1D laminar flame simulations. While this is a useful tool to infer temperatures in the products and lean regions where variations in γ/W are below 7%, variations in the rich side are an order of magnitude larger due to large molecular weight gradients in the vicinity of the hydrogen inlet. Joint simulations or Raman measurements can help address this challenge.
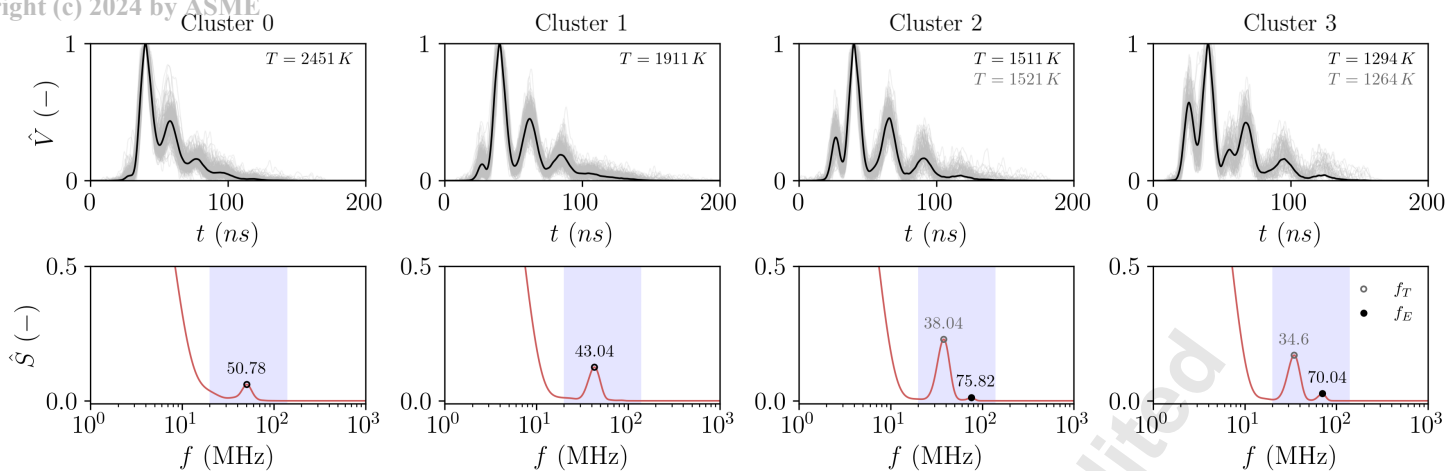
Figure 7: Four main LIGS modes obtained using k-means clustering (8 clusters, best of 100 initializations) at the location $z = 95$ mm, $r = 40$ mm. (Top:) LIGS spectra in normalized voltage $\hat{V}$ vs. time format. Gray signals correspond to the raw data, with the mean LIGS spectrum traced in black color. (Bottom:) Corresponding normalized PSDs $\hat{S}$ of the mean spectrum as function of frequencies (in semi-logarithmic scale). The expected range of frequencies according to 1D simulations is highlighted in blue color. Electrostrictive and thermal peaks are indicated using filled and unfilled circles respectively. Temperatures measured from the highlighted frequencies are provided next to the corresponding LIGS spectra, in corresponding colors.

- *Data-driven approaches for stratified environments*: The LIGS technique performs the best in well-mixed and relatively homogeneous regions. This is evidenced by the low spread in temperature measurements in the products at the most downstream location $z = 95$ mm (Fig. 6). In the vicinity of shear layers (i.e., hydrogen/air, hydrogen/IRZ, air/ORZ), fluctuations in local temperature and species due to turbulent swirling motion yield a wide spectrum of LIGS signatures at the same location. The inherent complexity of these stratified environments poses a challenge to the technique which detects more than one temperature "mode" at the same location (i.e., at $z = 55$ mm, $r = 0$ mm in Fig. 6). The presence of multiple modes can also complicate the classification of LIGS frequencies as thermal or electrostrictive, as discussed in sec. 4.4. Frequency thresholds have so far been chosen *a posteriori* to separate thermal and electrostrictive signatures [29]. A more systematic and data-driven approach consists in grouping similar instantaneous LIGS signals into representative clusters to better isolate the different modes at the same location. They can then be used to infer the nature of the mechanism (thermal or electrostrictive).

As a proof-of-concept, a time-series clustering operation is applied to signals at the location ($z = 95$ mm, $r = 40$ mm) using scikit-learn's implementation of the k-means clustering algorithm [38]. This iterative algorithm partitions the data into k clusters such that the sum of within-cluster variances is minimized [39]. Over 1,000 LIGS spectra are partitioned into 8 representative clusters and the four most probable ones, making up 83% of the data (830 spectra), are shown in Fig. 7. The four spectra span a large range of temperatures between 2,500 and 1,250 K from hot combustion products exhibiting a pure thermal peak (clusters 0 and 1) to

a mixture of water and air at moderate temperatures exhibiting an additional electrostrictive signature (clusters 2 and 3). In fact, the transition from cluster 0 to cluster 3 illustrates a gradual descent along the slope of the $T(f_E)$ curve in Fig. 2, starting from the peak ($Z = Z_{st}$) and progressing into lower values of f_E. This demonstrates the potential of data-driven techniques in isolating the various temperature modes in turbulent stratified hydrogen flames, and is a promising avenue for future research endeavors.

6. CONCLUSION

Laser-induced grating spectroscopy was applied, for the first time, to a swirl-stabilized hydrogen-air flame in a high-pressure gas turbine facility. Spatio-temporal temperature measurements are conducted at 35 axial/radial locations in the non-premixed combustor using a portable LIGS unit. A conditioned processing methodology based on 1D laminar flame simulations is used to infer temperatures from experimentally-measured LIGS frequencies. Temperatures as high as 2,500 K are measured in the hot combustion product region of the flame, and constitute the highest temperatures ever measured using LIGS. This makes it an ideal diagnostic for thermometry of exhaust gases in hydrogen-powered combustors. A number of challenges arose, however, in the hydrogen-rich region of the flame due to large molecular weight gradients and mixing with hot combustion products and vitiated air. Pump pulse energies higher than 35 mJ are likely needed to achieve high signal-to-noise ratio measurements in these regions to obtain longer-lived gratings and improve the accuracy of temperature measurements. The application of data-driven clustering techniques on LIGS data of turbulent stratified environments is discussed and its potential in highlighting the different modes at each location is demonstrated using a state-of-the-art iterative algorithm.

ACKNOWLEDGMENTS

REFERENCES

[1] Bell, Stuart R. and Gupta, Manishi. "Extension of the Lean Operating Limit for Natural Gas Fueling of a Spark Ignited Engine Using Hydrogen Blending". In: *Combust. Sci. Technol.* 123.1–6 (Jan. 1997), pp. 23–48. ISSN: 0010-2202, 1563-521X. DOI: 10.1080/00102209708935620. URL: http://www.tandfonline.com/doi/abs/10.1080/00102209708935620.

[2] Schefer, R W. "Hydrogen enrichment for improved lean flame stability". In: *Int. J. Hydrogen Energy* (2003), p. 11.

[3] Halter, F, Chauveau, C, and Gokalp, I. "Characterization of the effects of hydrogen addition in premixed methane/air flames". In: *Int. J. Hydrogen Energy* 32.13 (Sept. 2007), pp. 2585–2592. ISSN: 03603199. DOI: 10.1016/j.ijhydene.2006.11.033. URL: https://linkinghub.elsevier.com/retrieve/pii/S0360319906005763.

[4] Degeneve, A., Mirat, C., Caudal, J., Vicquelin, R., and Schuller, T. "Effects of Swirl on the Stabilization of Non-Premixed Oxygen-Enriched Flames Above Coaxial Injectors". en. In: *ASME J. Eng. Gas Turbines Power* 141.12 (Dec. 2019), p. 121018. ISSN: 0742-4795, 1528-8919. DOI: 10.1115/1.4045024. URL: https://asmedigitalcollection.asme.org/gasturbinespower/article/doi/10.1115/1.4045024/1047003/Effects-of-Swirl-on-the-Stabilization-of.

[5] Candel, Sébastien, Durox, Daniel, Schuller, Thierry, Bourgouin, Jean-François, and Moeck, Jonas P. "Dynamics of Swirling Flames". In: *Annu. Rev. Fluid Mech.* 46.1 (2014), pp. 147–173. DOI: 10.1146/annurev-fluid-010313-141300.

[6] Candel, Sébastien, Durox, Daniel, Schuller, Thierry, Palies, Paul, Bourgouin, Jean-François, and Moeck, Jonas P. "Progress and challenges in swirling flame dynamics". In: *C. R. Méc.* 340.11 (2012), pp. 758–768. ISSN: 1631-0721. DOI: https://doi.org/10.1016/j.crme.2012.10.024.

[7] Gaydon, A. G. *The Spectroscopy of Flames*. en. Dordrecht: Springer Netherlands, 1974. ISBN: 978-94-009-5722-0. DOI: 10.1007/978-94-009-5720-6. URL: http://link.springer.com/10.1007/978-94-009-5720-6.

[8] Seitzman, Jerry M., Kychakoff, George, and Hanson, Ronald K. "Instantaneous temperature field measurements using planar laser-induced fluorescence". EN. In: *Optics Letters* 10.9 (Sept. 1985), pp. 439–441. ISSN: 1539-4794. DOI: 10.1364/OL.10.000439.

[9] Barlow, Robert S. "Laser diagnostics and their interplay with computations to understand turbulent combustion". en. In: *Proc. Combust. Inst.* 31.1 (Jan. 2007), pp. 49–75. ISSN: 15407489. DOI: 10.1016/j.proci.2006.08.122.

[10] Fuest, Frederik, Barlow, Robert S., Chen, Jyh-Yuan, and Dreizler, Andreas. "Raman/Rayleigh scattering and CO-LIF measurements in laminar and turbulent jet flames of dimethyl ether". en. In: *Combust. Flame* 159 (Aug. 2012), pp. 2533–2562. ISSN: 00102180. DOI: 10.1016/j.combustflame.2011.11.001.

[11] Hanson, R. K. and Davidson, D. F. "Recent advances in laser absorption and shock tube methods for studies of combustion chemistry". In: *Prog. Energy Combust. Sci.* 44 (Oct. 2014), pp. 103–114. ISSN: 0360-1285. DOI: 10.1016/j.pecs.2014.05.001.

[12] Goldenstein, Christopher S., Spearrin, R. Mitchell, Jeffries, Jay. B., and Hanson, Ronald K. "Infrared laser-absorption sensing for combustion gases". In: *Prog. Energy Combust. Sci.* 60 (May 2017), pp. 132–176. ISSN: 0360-1285. DOI: 10.1016/j.pecs.2016.12.002.

[13] Daily, John W. "Laser induced fluorescence spectroscopy in flames". In: *Prog. Energy Combust. Sci.* 23.2 (Jan. 1997), pp. 133–199. ISSN: 0360-1285. DOI: 10.1016/S0360-1285(97)00008-7.

[14] Dibble, R. W. and Hollenbach, R. E. "Laser rayleigh thermometry in turbulent flames". In: Eighteenth Symposium (International) on Combustion 18 (Jan. 1981), pp. 1489–1499. ISSN: 0082-0784. DOI: 10.1016/S0082-0784(81)80151-8.

[15] Yuen, Frank T.C. and Gülder, Ömer L. "Premixed turbulent flame front structure investigation by Rayleigh scattering in the thin reaction zone regime". en. In: *Proc. Combust. Inst.* 32.2 (2009), pp. 1747–1754. ISSN: 15407489. DOI: 10.1016/j.proci.2008.08.005.

[16] Skiba, Aaron W., Carter, Campbell D., Hammack, Stephen D., and Driscoll, James F. "Premixed flames subjected to extreme levels of turbulence part II: Surface characteristics and scalar dissipation rates". en. In: *Combust. Flame* 239 (May 2022), p. 111703. ISSN: 00102180. DOI: 10.1016/j.combustflame.2021.111703.

[17] Kaiser, Sebastian A. and Frank, Jonathan H. "Imaging of dissipative structures in the near field of a turbulent non-premixed jet flame". en. In: *Proc. Combust. Inst.* 31.1 (Jan. 2007), pp. 1515–1523. ISSN: 15407489. DOI: 10.1016/j.proci.2006.08.043.

[18] Roy, Sukesh, Gord, James R., and Patnaik, Anil K. "Recent advances in coherent anti-Stokes Raman scattering spectroscopy: Fundamental developments and applications in reacting flows". In: *Prog. Energy Combust. Sci.* 36.2 (Apr. 2010), pp. 280–306. ISSN: 0360-1285. DOI: 10.1016/j.pecs.2009.11.001.

[19] Stampanoni-Panariello, A., Kozlov, D. N., Radi, P. P., and Hemmerling, B. "Gas-phase diagnostics by laser-induced gratings II. Experiments". In: *Appl. Phys. B* 81.1 (July 2005), pp. 113–129. ISSN: 1432-0649. DOI: 10.1007/s00340-005-1853-y.

[20] Stampanoni-Panariello, A., Kozlov, D. N., Radi, P. P., and Hemmerling, B. "Gas phase diagnostics by laser-induced gratings I. theory". en. In: *Appl. Phys. B* 81 (July 2005), pp. 101–111. ISSN: 0946-2171, 1432-0649. DOI: 10.1007/s00340-005-1852-z.

[21] Cummings, E. B. "Laser-induced thermal acoustics: simple accurate gas measurements". In: *Opt. Lett.* 19.17 (Sept. 1994), pp. 1361–1363. DOI: 10.1364/OL.19.001361.

[22] Kiefer, Johannes and Ewart, Paul. "Laser diagnostics and minor species detection in combustion using resonant four-wave mixing". In: *Prog. Energy Combust. Sci.* 37.5 (2011), pp. 525–564. ISSN: 0360-1285. DOI: https://doi.org/10.1016/j.pecs.2010.11.001.

[23] Gutfleisch, M., Shin, D.I., Dreier, T., and Danehy, P.M. "Mid-infrared laser-induced grating experiments of C2H4 and NH3 from 0.1–2 MPa and 300–800 K". In: *Appl. Phys. B* 71.5 (Nov. 2000), pp. 673–680. ISSN: 1432-0649. DOI: 10.1007/s003400000408.

[24] De Domenico, Francesca, Guiberti, Thibault F., Hochgreb, Simone, Roberts, William L., and Magnotti, Gaetano. "Temperature and water measurements in flames using 1064 nm Laser-Induced Grating Spectroscopy (LIGS)". en. In: *Combust. Flame* 205 (July 2019), pp. 336–344. ISSN: 00102180. DOI: 10.1016/j.combustflame.2019.04.016. URL: https://linkinghub.elsevier.com/retrieve/pii/S0010218019301610.

[25] Ruchkina, Maria, Hot, Dina, Ding, Pengji, Hosseinnia, Ali, Bengtsson, Per-Erik, Li, Zhongshan, Bood, Joakim, and Sahlberg, Anna-Lena. "Laser-induced thermal grating spectroscopy based on femtosecond laser multi-photon absorption". en. In: *Sci. Rep.* 11.11 (May 2021), p. 9829. ISSN: 2045-2322. DOI: 10.1038/s41598-021-89269-2. URL: https://www.nature.com/articles/s41598-021-89269-2.

[26] Sahlberg, Anna-Lena, Hot, Dina, Kiefer, Johannes, Aldén, Marcus, and Li, Zhongshan. "Mid-infrared laser-induced thermal grating spectroscopy in flames". In: *Proc. Combust. Inst.* 36.3 (Jan. 2017), pp. 4515–4523. ISSN: 1540-7489. DOI: 10.1016/j.proci.2016.07.017.

[27] Luers, Andrew, Salhlberg, Anna-Lena, Hochgreb, Simone, and Ewart, Paul. "Flame thermometry using laser-induced-grating spectroscopy of nitric oxide". en. In: *Appl. Phys. B* 124.3 (Feb. 2018), p. 43. ISSN: 1432-0649. DOI: 10.1007/s00340-018-6912-2.

[28] Hot, Dina, Sahlberg, Anna-Lena, Aldén, Marcus, and Li, Zhongshan. "Mid-infrared laser-induced thermal grating spectroscopy of hot water lines for flame thermometry". In: *Proc. Combust. Inst.* 38 (Jan. 2021), pp. 1885–1893. ISSN: 1540-7489. DOI: 10.1016/j.proci.2020.06.289.

[29] Weller, Lee, Shah, Priyav, Giles, Anthony, De Domenico, Francesca, Morris, Steve, Williams, Benjamin AO, and Hochgreb, Simone. "Spatial temperature and water molar concentration measurements using thermal and electrostrictive LIGS during operation of a swirl burner at pressure". In: *ASME Turbo Expo*. Vol. 86977. American Society of Mechanical Engineers. 2023, V004T05A004.

[30] Shah, Priyav, Le Page, Laurent M, and Williams, Benjamin AO. "Development and characterization of PILOT: a transportable instrument for laser-induced grating spectroscopy". In: *Opt. Express* 31.4 (2023), pp. 5872–5881.

[31] Runyon, Jon, Marsh, Richard, Bowen, Philip, Pugh, Daniel, Giles, Anthony, and Morris, Steven. "Lean methane flame stability in a premixed generic swirl burner: Isothermal flow and atmospheric combustion characterization". In: *Exp. Therm. Fluid Sci.* 92 (2018), pp. 125–140.

[32] Pugh, Daniel, Bowen, Philip, Crayford, Andrew, Marsh, Richard, Runyon, Jon, Morris, Steven, and Giles, Anthony. "Catalytic influence of water vapor on lean blow-off and NOx reduction for pressurized swirling syngas flames". In: *ASME J. Eng. Gas Turbines Power* 140.6 (2018).

[33] Pugh, Daniel, Bowen, Philip, Valera-Medina, Agustin, Giles, Anthony, Runyon, Jon, and Marsh, Richard. "Influence of steam addition and elevated ambient conditions on NOx reduction in a staged premixed swirling NH3/H2 flame". In: *Proc. Combust. Inst.* 37.4 (2019), pp. 5401–5409.

[34] Goodwin, David G., Moffat, Harry K., Schoegl, Ingmar, Speth, Raymond L., and Weber, Bryan W. *Cantera: An Object-oriented Software Toolkit for Chemical Kinetics, Thermodynamics, and Transport Processes*. https://www.cantera.org. Version 2.6.0. 2022.

[35] Ranzi, E., Frassoldati, A., Grana, R., Cuoci, A., Faravelli, T., Kelley, A. P., and Law, C. K. "Hierarchical and comparative kinetic modeling of laminar flame speeds of hydrocarbon and oxygenated fuels". In: *Prog. Energy Combust. Sci.* 38.4 (Aug. 2012), pp. 468–501. ISSN: 0360-1285. DOI: 10.1016/j.pecs.2012.03.004. URL: https://www.sciencedirect.com/science/article/pii/S0360128512000196.

[36] Ranzi, Eliseo, Frassoldati, Alessio, Stagni, Alessandro, Pelucchi, Matteo, Cuoci, Alberto, and Faravelli, Tiziano. "Reduced Kinetic Schemes of Complex Reaction Systems: Fossil and Biomass-Derived Transportation Fuels". en. In: *Int. J. Chem. Kinet.* 46.9 (2014), pp. 512–542. ISSN: 1097-4601. DOI: 10.1002/kin.20867. URL: https://onlinelibrary.wiley.com/doi/abs/10.1002/kin.20867.

[37] Ranzi, Eliseo, Cavallotti, Carlo, Cuoci, Alberto, Frassoldati, Alessio, Pelucchi, Matteo, and Faravelli, Tiziano. "New reaction classes in the kinetic modeling of low temperature oxidation of n-alkanes". In: *Combust. Flame* 162.5 (May 2015), pp. 1679–1691. ISSN: 0010-2180. DOI: 10.1016/j.combustflame.2014.11.030. URL: https://www.sciencedirect.com/science/article/pii/S0010218014003848.

[38] Pedregosa, F., Varoquaux, G., Gramfort, A., Michel, V., Thirion, B., Grisel, O., Blondel, M., et al. "Scikit-learn: Machine Learning in Python". In: *J. Mach. Learn. Res.* 12 (2011), pp. 2825–2830.

[39] Murphy, Kevin P. *Probabilistic Machine Learning: An introduction*. MIT Press, 2022. URL: probml.ai.